HiSST: 3rd International Conference on
High-Speed Vehicle Science Technology
14 -19 April 2024, Busan, Korea

Simulation of DC gliding arcs for supersonic combustion: influence on O_2/H_2 ignition

A. Rocamora [1], F. Tholin [1], A. Bourlet [1], J. Labaune [1], C. O. Laux [2]

Abstract

The scramjet engine has been developed to reach high Mach number flight. However, supersonic combustion is difficult to initiate and sustain in a reasonable engine size. In addition to the cavity, strut or step flame holders, PAC (Plasma-Assisted Combustion) is another possibility to stabilize the combustion. This article is dedicated to a particular plasma technology: the Q-DC (Quasi-Direct Current) gliding arc, which creates high temperature regions at about 10 000 K in the fuel mixing zone. The study is based on an adaptation of S. B. Leonov's PIM (Plasma Injector Module) in a Mach 2 flow. To model PAC, the Navier-Stokes equations with Joule heating and the electric-field are solved by two coupled codes. The restrike phenomenon is taken into account, thanks to a plasma discharge macromodel. The combustion of H_2/O_2 is modeled by a skeletal 9-species kinetic mechanism. This paper demonstrates the capacity of the electric arc to ignite and maintain combustion in unfavourable conditions.

Keywords: *scramjet, Plasma-assisted combustion, DC-gliding arc, kinetics, hydrogen combustion, supersonic combustion, restrike*

Nomenclature

Latin
T_i – Inlet temperature [K]
P_i – Inlet pressure [Pa]
$\dot{m}$ – Mass flux [g·s^{-1}]
Y_k – Mass fraction of species k [-]
I – Current intensity [A]
U – Voltage [V]
WT– heat release [W·m^{-3}]
Greek
σ – Electric conductivity [S·m^{-1}]
Superscripts
$\bar{q}$ – Time average of q quantity

1. Introduction

Recent research has focused on economically viable solutions for very long distance passenger transportation [1]. Hypersonic flight upper than Mach 5 for airbreathing aircraft is not reachable with classic turbo engines, not even with ramjet engines. A scramjet engine is needed. Like the ramjet, it has no moving parts, but the combustion reaction occurs in a supersonic flow. In such conditions, the residence time is very short, and the combustion can be unstable at Mach numbers above 5 and altitudes higher than 20 km [2]. For decades, many techniques have been developed to control combustion. These can be divided into two categories: intrusive and non-intrusive flame holders. Examples of intrusive technologies are strut [3] and pylon [4], while step [5] and cavity [6] are considered non-intrusive, with the possibility of using them together [7], [8]. A substantial intrusion can slow down the flow, which is inefficient for hypersonic flights. On the contrary, if fuel-air mixing is insufficient, the combustion can start too late, and thus become ineffective. For this reason, developing non-intrusive and effective flame holders is still a challenging issue for supersonic combustion. A

[1] *ONERA, Université Paris Saclay, 91120, Palaiseau, France, surname.name@onera.fr*
[2] *Laboratoire EM2C CNRS-CentraleSupélec, Université Paris-Saclay, Gif-sur-Yvette – France, christophe.laux@centralesupelec.fr*

promising technology that can be used alone or in combination with other devices relies on plasma-assisted combustion (PAC). Several types of plasma have been tested: sparks [9], plasma torches [10], and Nanosecond Repetitively Pulsed (NRP) discharges [11]. The plasma generation method chosen in this paper is a Quasi-Direct Current (Q-DC) discharge near the wall. High-voltage electrodes placed in the combustor generate plasma that enhances the chemical kinetics by depositing energy and stabilising the combustion like a classical flame holder.

Section 2 presents the combustor and the plasma module as well as the coupling strategy, the meshes used and the applied boundary conditions. Section 3 describes the plasma-flow coupling and the arc's effect on combustion. Preliminary results are presented about the placement and chemical kinetics induced by the arc.

This work simulates the capability of such an electric arc coupled with the flow to ignite and maintain H_2-air combustion in unfavourable conditions of pressure and temperature.

2. Numerical setup

2.1. Facility design

The Q-DC arc has been tested with H_2 fuel injection, especially on the LAPCAT-II combustor operated in the LAERTE facility of ONERA Palaiseau Research Center [12]. The geometry of combustor presented in Fig 1 and described with more details in [13], is used for the simulation. The X-axis reference is positioned at the throat of the Mach 2 nozzle. The combustor has three sections: 65 mm < x_1 <280 mm < x_2 < 598 mm < x_3 < 648 mm with respectively constant, 1°, and 3° diverging angles. The injector is located at X = 200 mm and its radius is 1 mm.

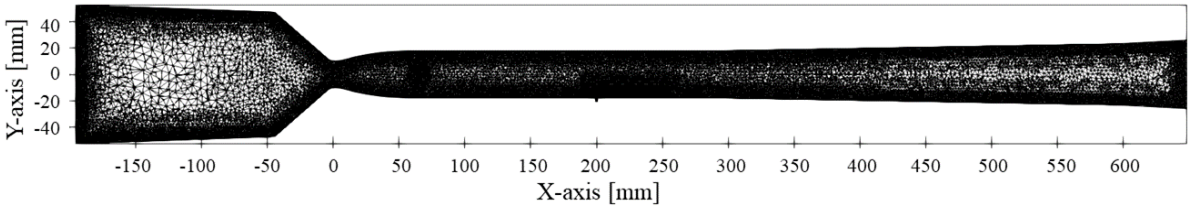

Fig 1. X-Y slice of the CEDRE mesh, including the tank, the 1 mm radius injector and the constant, 1° and 3° diverging angle test-sections.

An original PIM (Plasma Injector Module) adapted from those developed by Leonov *et al.* [14], [15], [16] is implemented on the combustor. As shown in Fig 2, it comprises an annular anode (in red) surrounding the injector (in blue) and insulated from the rest of the combustor wall (in green) by a ceramic with an obovate shape (in orange). This specific architecture has the advantage of ensuring that the upstream arc root remains attached close to the point of fuel injection, while the arc is free to move downstream at the fuel-air interface, thus enhancing the combustion.

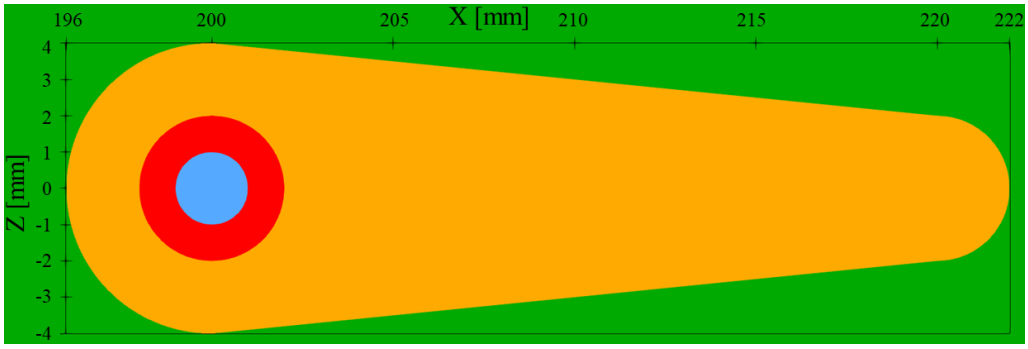

Fig 2. Schematic of PIM. In blue the injector fluid part, in green the cathode, in orange the ceramic and in red the anode. The shape is inspired similar to the PIM proposed by Leonov *et al.*.

Despite the many experimental studies that have been conducted, there are not many simulations of PAC with Q-DC gliding arcs because of the stiff physical coupling between the flow and the plasma dynamics. A second difficulty results from the multi-scale nature of plasma-flow interactions: small time steps of the order of 1 microsecond are required to solve the coupled dynamics while the simulation

time of interest in PAC is of a few milliseconds. A similar problematic arises for space discretization, with cell sizes of the order of 1 mm and a test-rig length of almost 1 m. In addition, 2D simulations cannot be performed due to the 3D structure of the flow and the plasma. Notably, 3D is of particular importance for the flow to be able to bypass the plasma, while 2D tends to overestimate the fraction of the flow crossing the arc.

2.2. Solvers

Two codes developed at the ONERA are coupled through the CWIPI library [17] to solve the fluid and electric equations.

The first code, named CEDRE [18], solves the Navier-Stokes equations and transport of species using a finite rate chemistry Large Eddy Simulation (LES) with a sub-mesh Smagorinsky model as simulated by G. Pelletier [19]. The combustion chemistry is modeled with the skeletal H_2/O_2 kinetic mechanism of Jachimowski [20]. It comprises 9 species (H_2, H_2O, N_2, O_2, OH, H, O, HO_2, H_2O_2) and 19 reactions neglecting N_2 dissociation. The heat capacity of the various species is calculated with a polynomial interpolation fit that is valid up to 20 000 K, making it possible to properly describe the very high temperature of the DC arc plasma.

The second code is TARANIS, a quasi-neutral plasma solver developed at ONERA. TARANIS computes the electric conductivity of the plasma and solves in parallel the electrostatic current conservation equation with Ohm's law thanks to the PETSc library [21]. As the currents involved are low, the magnetic field is neglected.

Temperature, pressure and velocity fields are sent from CEDRE to TARANIS as described in Fig 3. TARANIS uses them to calculate the gas conductivity and the electric field. The calculation of the plasma conductivity is based on the work of D'Angola [22] considering pure air at LTE (Local Thermal Equilibrium), thus neglecting non equilibrium effects in the plasma and the influence of hydrogen in the mixture. In future works a consistent LTE conductivity that would be valid for any H_2/air/H_2O mixtures will be computed. However, as a first step, the pure air LTE assumption for the conductivity seems reasonable since the presence of H_2 or H_2O is not expected to have a large influence due to the high dissociation and ionization degree in the plasma. Then, TARANIS calculates the Joule heating used as a source term in the energy conservation equation in CEDRE for the next iteration.

Experiments on DC arcs reveal that their spatial extent is controlled by a "restrike" phenomena, which corresponds to the very fast formation of a field-induced plasma channel between two arc branches as the arc is stretched by the flow. To address this complex but yet essential discharge phenomenon, the restrike model developed by Bourlet *et al.* [23], [24] is used in the presented simulations. The restrike model takes as an input parameter the reduced breakdown field in the considered gas, which is assumed to be the breakdown field of pure air in this study, *ca.* 30 kV·cm^{-1}, *i.e.* 123 Td in standard condition. In future work this reduced breakdown field will be refined by considering the exact gas composition in the H_2/air mixture.

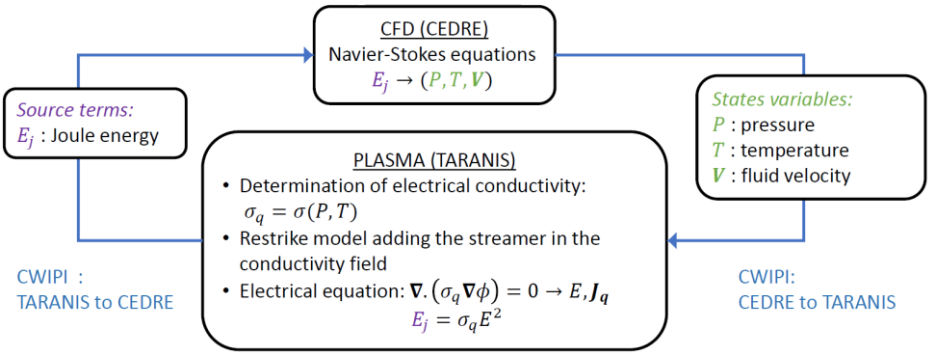

Fig 3. Coupling scheme between CEDRE and TARANIS with CWIPI library. For each iteration, CEDRE sends states variables to TARANIS. In return, it provides the heat source term to CEDRE.

2.3. Meshing

CEDRE and TARANIS use two different meshes. For CEDRE, as shown in Fig 1, the tetrahedral cell size is 1 mm for most of the mesh and 200 µm for cells in the refined volume close to the injector. A total

of 15 million cells are used to mesh the LAPCAT-II geometry. The refined volume is the same for CEDRE and TARANIS. To ensure a maximal $y^+$of 5 at the combustion chamber walls, the boundary layer mesh is 0.75 mm thick.

An X-Y slice of the mesh used in Taranis is shown on Fig 4. The part in blue is the fluid domain which is coincident with the mesh used by CEDRE around the PIM and the injector. To properly solve the current and electric field distributions, solid domains corresponding to the electrodes and the insulating materials must be included in TARANIS while they are not present in CEDRE. The red part in Fig 4 corresponds to the anode, the green part to the cathode and the orange part to the insulating ceramics of the PIM. The solid domain is 3 mm thick with refined cells of 2.54 µm thickness close to the fluid-solid interface in order to resolve the electric field distribution at the boundaries.

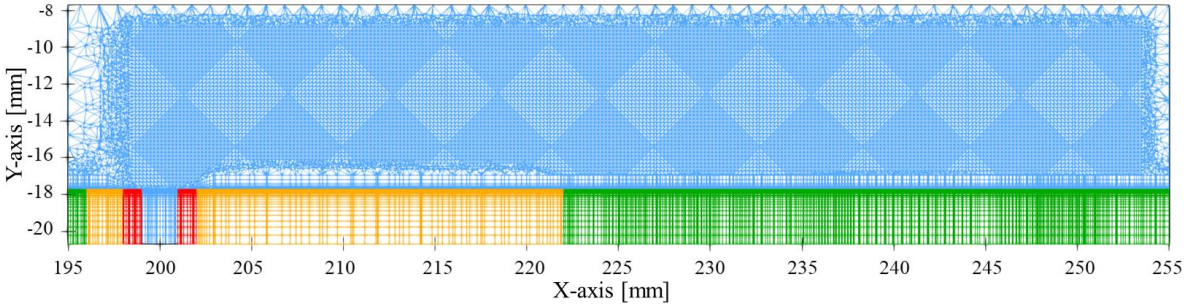

Fig 4. Slice in X-Y plane of TARANIS mesh with both the fluid and the wall region. In blue the fluid part (same mesh as in CEDRE), in green the cathode, in orange the ceramic and in red the anode.

2.4. Boundary conditions

Boundary conditions are specific for each code, as described in Table 1. To reproduce the experimental global air-fuel equivalence ratio condition of 0.15 used in [19], a pressure of P_i = 4 bar and a temperature of T_i = 1 400 K are imposed at the entrance of the duct. To obtain this condition in the LAPCAT-II bench, the air is heated by two H_2 burners, while pure O_2 is also upstream injected to keep the desired Y_{O_2}. The consequence is an injection of vitiated air containing 13.5% of H_2O, 61.5% of N_2 and 25% of O_2. This proportion is kept for the mass fraction input. During the simulations the temperature of the wall is maintained at 700 K. An H_2 flowrate of 1.5 g·s^{-1} is chosen for the injector. The supersonic outlet means that no state variables are imposed on the boundary.

For TARANIS, material conductivities are defined in addition of current and voltage. For the electrodes, a 10^7 S·m^{-1} conductivity, which is a rough estimation for metal, is retained. The air conductivity is calculated from tables but a minimal value is set at 10^{-3} S·m^{-1}. For the ceramic, the conductivity is set to a low value to prevent current leak: σ = 10^{-6} S·m^{-1}. The current and the maximum voltage are set to the experimental values for one PIM taken from [15], which deals with hydrogen combustion.

Table 1. Fluid and electric boundary condition

CEDRE	**Inlet**	P_i = 4 bar T_i = 1 400 K	Y_{N_2} = 0.615 Y_{O_2} = 0.25 Y_{H_2O} = 0.135
	Wall	T = 700 K	
	Injector	Subsonic inlet	$\dot{m}_{H_2}$ = 1.5 g·s^{-1}
	Outlet	Supersonic outlet	
TARANIS	**Fluid**	σ_{min} = 10^{-3} S·m^{-1}	
	Anode	σ = 10^7 S·m^{-1}	I = 5 A V_{max} = 5 kV
	Cathode		U = 0 V
	Ceramic	σ = 10^{-6} S·m^{-1}	I = 0 A

3. Results

This section presents the results of the coupled TARANIS and CEDRE simulation. The total simulated time with plasma-on is 3.7 ms, which is enough to ignite combustion and stabilize the combustion. The time step is 10^{-8} s for the first 0.26 µs (duration of the transient regime during which the first arc connects the electrodes), and then extended to 10^{-7} s for the following iterations.

The absolute average error on the simulated electric current is $3 \cdot 10^{-3}$ A with a standard deviation of $2 \cdot 10^{-2}$ A. For this work, the use of restrike is space limited 1.5 mm above the Y-axis. This can slow down the movement of the downstream arc root, by prohibiting restrikes between this root and cathode and gives to it a longer length.

3.1. Plasma and flow

The goal of this section is to explore plasma-flow interactions. The Fig 5 brings an idea of the arc's morphology as described in [25] by three dimensional reconstruction from experimental results.

According to the experimental results, the maximal extent of the arc is about 50 mm, which is twice the ceramic length. The upstream root of the arc (anode) shows small oscillations in position. The convected downstream root moves regularly from one side of the ceramic to the other. The fact that the electric arc does not always anchor itself on the same side of the ceramic is an advantage for combustion because the arc sweeps a larger volume of the combustion mixture.

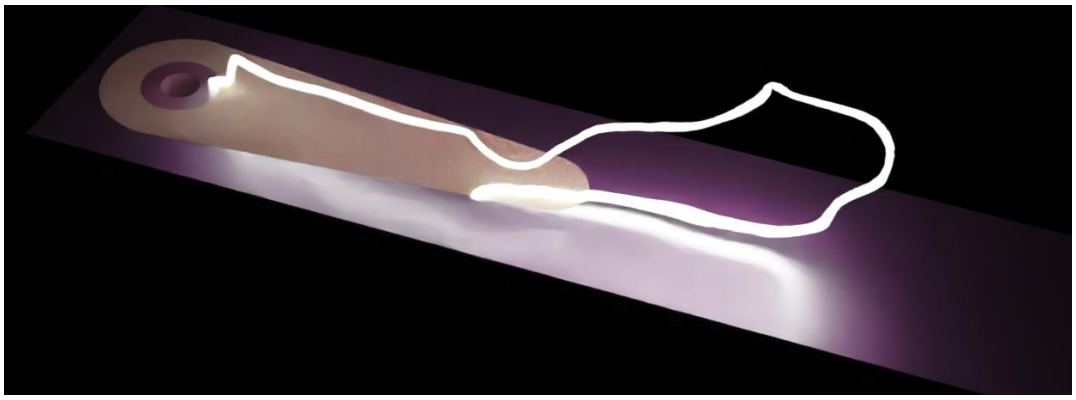

Fig 5. Simulation of the Q-DC arc obtained with the PIM device in the LAPCAT-II test-rig. Realistic rendering of the fully extended arc convected by the flow before restrike. As in experiments, the left arc root is connected to the anode, while the right arc root moves freely around the PIM.

Fig 6 shows a superposition of numerical Schlieren images showing the density gradients (in grey) and of the arc contour (defined as the regions where the temperature is above 8 000 K). The three X-Y slices are chosen for different Z coordinates to stay centered on the interesting part of the arc.

The left image shows the region of the H_2 injector, located at X = 200 mm. The figure shows that the upstream arc root is attached downstream of the Mach disk produced by the injected jet of H_2. The arc quickly growths vertically by about 5 mm.

The middle part of Fig 6 shows that the arc extends horizontally downstream, at a distance above the wall of about 5 mm, *i.e.* just below the edge of the mixing layer.

The right part of the Fig 6 shows that the mixing layer is more turbulent. The arc is entrained by the vortices, giving it the downstream big curl. During the arc transport, the downstream root of the arc stays confined within the flow boundary layer while the rest of the arc is convected in the mixing layer.

As the arc is crossed by the flow, its electrical resistance grows. The voltage oscillates between 0 and 2 kV. Since the current is fixed at 5 A, the power is proportional to the voltage and varies between 0 and 10 kW with an average value around 2.5 kW. The absolute average error on the current is 0.3% of the input current with a standard deviation of 2%.

The voltage peak at 0 ms in Fig 7 is caused by the absence of a conductive channel between the anode and cathode during the first iteration, the model being activated after the electric field has been initialised. The sudden variations in voltage are due to restrikes as the voltage varies with the arc

length. In this 3.7 ms simulation, the restrike model was activated 901 times to generate streamers, but the streamers converted to arcs in only 72 case. Thus, the restrike frequency is 19 kHz for this simulation.

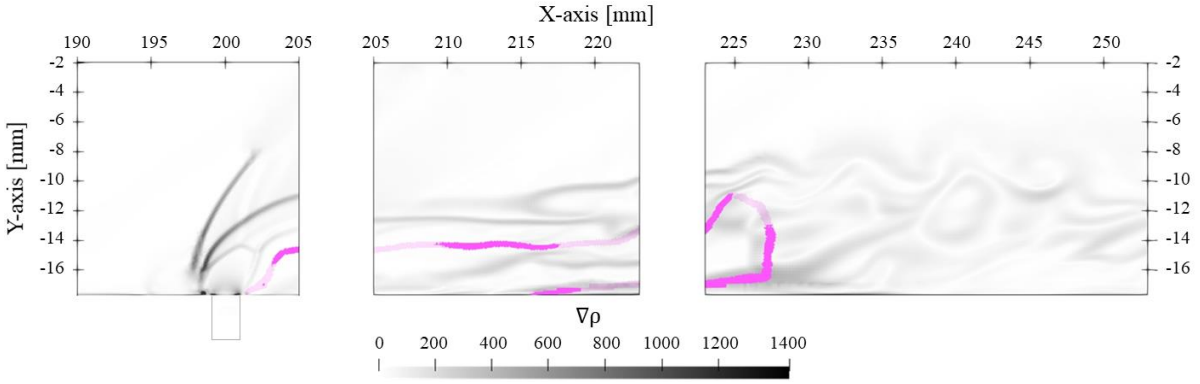

Fig 6. Transparent numerical-Schlieren of X-Y slice of ∇ρ at 3 Z-axis representative arc positions: upstream root (left), horizontal development (middle) and downstream root (right). The arc corresponds to T = 8 000 K.

Fig 7 shows the voltage variations and the volume heated by the arc (defined as the region where the temperature is above 3 000 K). The oscillations are due to the restrikes. It should be noted, however, that for the figure not all restrikes are visible because the volume is calculated only every 100 iterations.

As time goes by, a phase shift between volume and voltage appears. It can be explained by the gas bulks heated over 3 000 K which are transported by the flow and persist after the arc restrike. The average volume heated by plasma is 49 mm^3, which means that the arc deposits 50 $W \cdot mm^{-3}$ on average in the combustor.

The fall of the heated volume below 40 mm^3 between 2 and 2.5 ms can be explained by a series of more frequent restrikes, limiting the arc length. This analysis is corroborated by the height of the voltage peaks, which are lower than in the rest of the simulation.

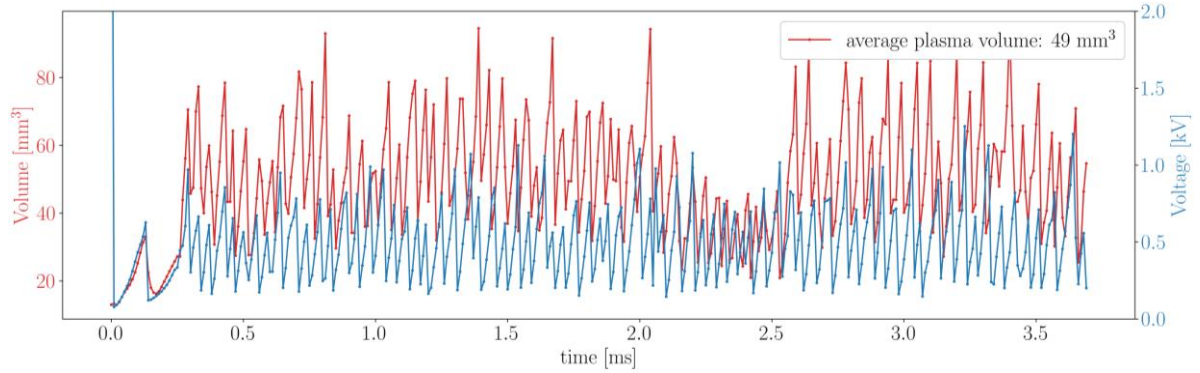

Fig 7. Evolution of the anode voltage and the plasma volume heated above 3 000 K.

3.2. Plasma-combustion interaction

Now the impact of the plasma on the combustion is examined. Fig 8 compares the injector wall pressure along the X-axis at Z = 0 mm from the throat to the exit nozzle with and without plasma. The overlap of the two curves between X = 0 mm and the injector at X = 200 mm indicates that the supersonic flow is well established. The plasma area is located between 200 and 250 mm.

Around 270 mm, the pressure peak caused by the second bow shock reflection is shifted upstream. This decreasing X-shift is attributed to the presence of the plasma, which acts as an obstacle in the flow and deflects the crossflow. This pressure peak is also slightly increased. It is due to the start of the combustion.

Then, from 300 mm to 700 mm, the pressure increases by about 0.015 MPa when the plasma is applied. This increase is the signature of combustion. The decrease in wall pressure is jointly due to the section diverging angle and exit of the combustion zone. The sudden drop of the pressure after 600 mm is due

to the 3° diverging angle.

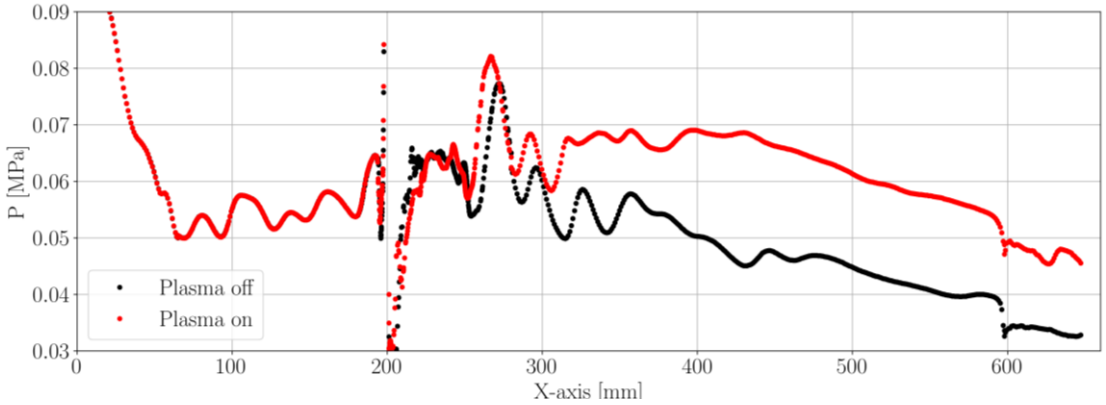

Fig 8. Static pressure distribution on the injector wall for two cases: plasma-on for 3.7 ms (red) and plasma-off (black).

Fig 9 shows a comparison of the temporal evolution of the space averaged heat release rate (WT) with and without plasma in the combustion. The plasma is turned on at time 0 ms.

The first part of simulation without plasma (red zone) at time lower than 0 ms, where the WT is approximately equal to 0, indicates that the mixture is not ignited at the chosen T_i and P_i. In fact, without plasma, for same simulation parameters with T_i = 1 500 K the combustion does not start.

On the contrary, adding plasma (green zone) successfully ignites the mixture, meaning that the plasma increases the temperature by at least at least several tens of Kelvin on the combustor operation domain. After 0.3 ms, the combustion is well established with WT oscillating between 100 and 120 kW and a time average of 108 kW. Knowing that the plasma power is 2.5 kW, the power ratio is less than 2.5%.

The deactivation of the plasma at 3.7 ms (second red zone) shows that plasma is not only useful for igniting combustion, but also to maintain it, since the WT falls to its previous value in less than 1 ms.

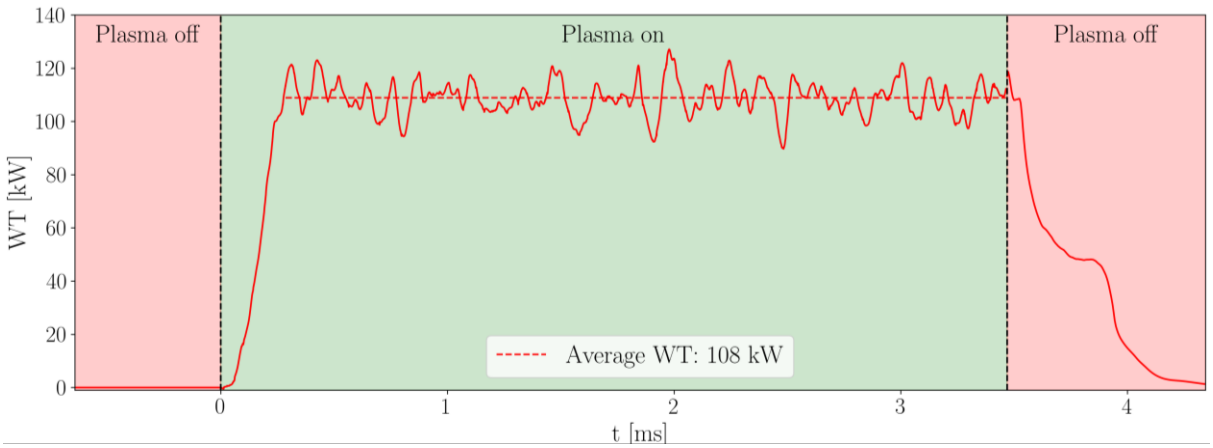

Fig 9. Temporal evolution of the space-averaged heat release WT in the combustor with (green zone) and without (red zone) plasma activation.

To have a better idea of where the combustion is taking place, Fig 10 shows $\overline{WT}$ and $\bar{T}$ on a X-Y slice. The arc triggers combustion between 200 mm and 240 mm, that is consistent with Fig 8. The maximum heat release is reached between 250 and 400 mm, where the flame occupies around 60% of the combustor cross-section at its maximum (X = 360 mm). The temperature reaches 2 000 K after X = 320 mm and stays constant until the combustor exit.

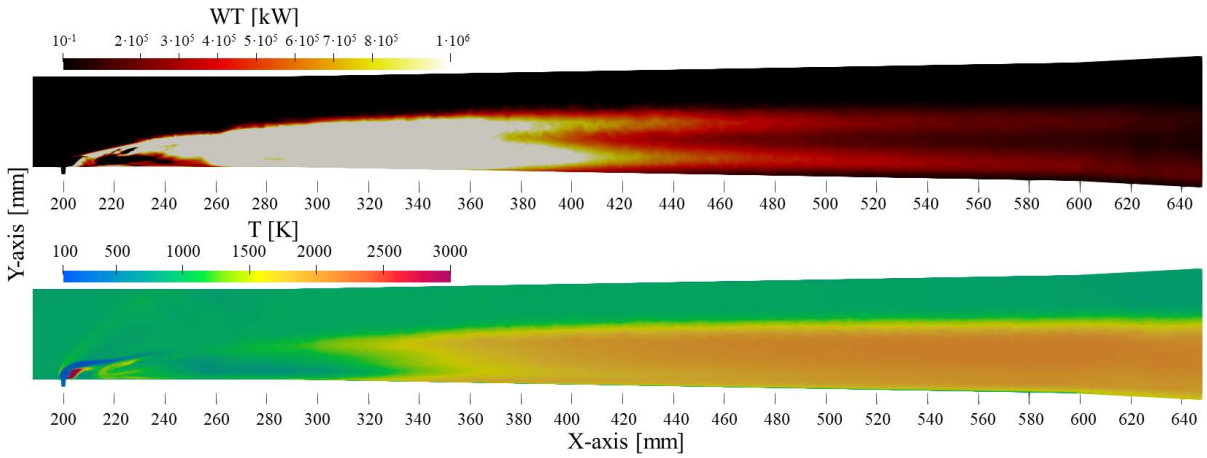

Fig 10. X-Y slice of $\overline{WT}$ rate (top) and $\bar{T}$ (bottom) after 3.7 ms of plasma actuation.

3.3. Arc position analysis

The ability of the electric arc to initiate and maintain combustion is the combination of two factors: its position at the fuel/oxidant interface and the gas heating: the core of the arc reaches 8 000 K. This temperature is sufficient to dissociate gas molecules but this must take place in a region where both the fuel and the oxidizer are present simultaneously.

Fig 11 shows three sections corresponding to the main arc characteristics (upstream root, horizontal development, downstream root). The H_2 mass fraction field indicates the penetration of the H_2 cross-flow into the main flow. The temperature contours show the influence area of the arc (arc regions at temperatures above 2 000 K). The flow structure with plasma (on the right) and without plasma (on the left) are compared to illustrate the flow modification induced by the arc. Slices are taken before the combustion, which begins after X = 240 mm.

At X = 203 mm, the upstream arc root has dissociated H_2, because its temperature is higher than 2 000 K. The arc is mostly in the crossflow jet and mostly creates H.

At X = 223 mm, the arc is horizontally developed. Its cross-section is smaller (less than 2 mm^2) but always in a medium H_2 mass-fraction zone (0.2 – 0.6) favourable to combustion. The arc is no longer centered. Instead, it is located near the edges of the jet as a result of the influence of the flow vortices. The global plasma-on and plasma-off H_2 distributions are quite similar, showing Kelvin-Helmholtz instabilities and counter-rotating vortex pairs. However, the vortex closest to the arc is blown up and pushed to the side. The hot temperature contour at the bottom of the middle right figure is the downstream arc root trapped in the boundary layer. This part of the arc has no influence on the combustion because there is no H_2 and the other produced radicals are too slow to interact with the jet.

At X = 233 mm, the arc is only present periodically because of restrikes, so its influence is lower. However, some hot kernels are always active. Compared with the plasma-off flow structures, those with the plasma-on are wider in the Z direction (ΔZ = 12 mm against 8 mm for plasma-off) but narrower in the Y direction (Y_{max} = -8 mm against -6 mm for plasma-off). Moreover, the Y_{H_2}-rich zone is more clearly divided into two parts and convected by larger structures. These two effects could maximize the mixing with O_2 molecules. Nevertheless, this interpretation should be confirmed with more systematic investigations at each time step.

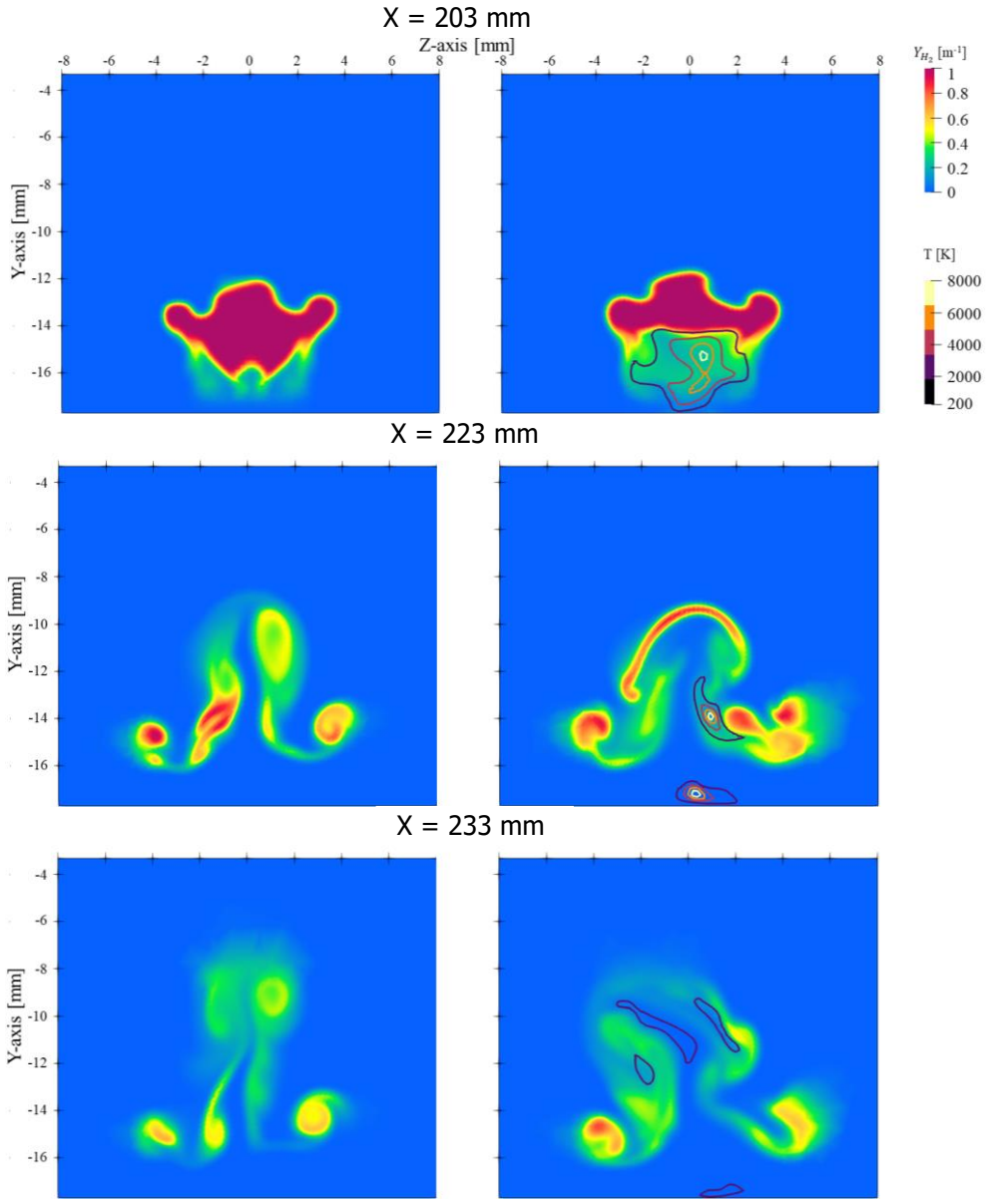

Fig 11. Y-Z slice of Y_{H_2} at X = 203, 223, 233 mm with plasma off (left) and plasma on (right). To locate the plasma in the plasma-on case, contour plots for different isotherms are depicted.

Table 2. Chemical composition of the cell with the highest temperature in the arc and at LTE

Species (%)	Y_H	Y_O	Y_{OH}	Y_{H_2}	Y_{H_2O}	Y_{O_2}	**T [K]** / **P[Pa]**
X=203 mm	13.95	8.05	12.44	18.64	6.23	0.22	10 000 / 33 000
LTE	33.97	25.59	0	0	0	0	
X=223 mm	8.54	8.99	15.82	12.97	9.07	5.32	9 000 / 40 000
LTE	23.46	32.54	0	0	0	0	
X=233 mm	4.4	18.16	13.8	2.89	3.35	1.75	10 000 / 60 000
LTE	8.5	36.01	0	0	0	0	

This analysis of plasma radicals production has to be shaded by the limit of kinetic scheme used. Table 2 reports the mass fractions of all species (except N_2, which is non-reactive and H_2O_2, HO_2, which have negligible mass fractions) in the highest temperature cell of the X = 203, 223, 233 mm slices.

A 0D calculation is also performed with the same composition, pressure, temperature and set of reactions until LTE is reached. The results prove that the species in the arc are not at the LTE. The O and H radicals are above and below, respectively, the LTE values. Because both can enhance the flame chemistry [26], [27], it is difficult to conclude on the influence of the kinetic mechanism on combustion ignition, at the moment.

Conclusion

PAC simulations have been performed of the LAPCAT-II Mach 2 scramjet bench equipped with a PIM Q-DC gliding arc actuator similar to the one of Leonov *et al.*. To this end, the reactive CFD solver CEDRE has been coupled to a quasi-neutral plasma solver TARANIS thanks to the coupling library CWIPI. The initial main flow temperature was set a few tens Kelvin below the auto-ignition temperature for a similar fuel equivalence ratio. The O_2/H_2 kinetic mechanism is adapted from Jachimowsky's work. The comparison between plasma-assisted and plasma-unassisted simulations of the heat release and wall pressure in the combustor shows significant differences. The arc successfully ignites and sustains the combustion during the 3.7 ms interval during which it is turned on. Once deactivated, the combustion stops in less than 1 ms, suggesting that the arc is necessary to maintain combustion by producing H, OH, and O radicals. The electric power needed to generate the arc generation represents 2.5% of the flame thermal power. As shown from the 3D simulations, the arc follows the vortices and maintains itself in a reactive region. At the same time, the structures of the mixing layer are modified by the arc.

Acknowledgments

The authors would like to thank the French Defense Innovation Agency (AID), the French Procurement Agency (DGA) and the ONERA's scientific direction for funding and supporting the present work.

References

[1] N. Viola *et al.*, 'H2020 STRATOFLY project : from Europe to Australia in less than 3 hours', presented at the ICAS 2021 THE 32 nd CONGRESS OF THE INTERNATIONAL COUNCIL OF THE AERONAUTICAL SCIENCES, Shanghai, China, Sep. 2021. [Online]. Available: https://hal.science/hal-03695156

[2] S. B. Leonov, D. Yarantsev, and V. Sabelnikov, 'Electrically driven combustion near the plane wall in a supersonic duct', in *Progress in Propulsion Physics*, Versailles, France: EDP Sciences, 2011, pp. 519–530. doi: 10.1051/eucass/201102519.

[3] G. Choubey, M. Solanki, O. Patel, Y. Devarajan, and W. Huang, 'Effect of different strut design on the mixing performance of H2 fueled two-strut based scramjet combustor', *Fuel*, vol. 351, no. 128972, Nov. 2023, doi: 10.1016/j.fuel.2023.128972.

[4] R. Balar, K. Yu, A. Gupta, and A. Kothari, 'Pylon-Aided Fuel Injection into Supersonic Flow', in *45th AIAA Aerospace Sciences Meeting and Exhibit*, Reno, Nevada: AIAA Paper 2007-834, Jan. 2007. doi: 10.2514/6.2007-834.

[5] J.-M. Klein, A. Gandilhon-Gounelle, A. Vincent-Randonnier, A. Genot, and A. Mura, 'On the invariance of flame-motion-induced variations of the generalized disturbance energy', *Combust. Flame*, vol. 251, p. 112711, May 2023, doi: 10.1016/j.combustflame.2023.112711.

[6] R. Moradi, A. Mahyari, M. Barzegar Gerdroodbary, A. Abdollahi, and Y. Amini, 'Shape effect of cavity flameholder on mixing zone of hydrogen jet at supersonic flow', *Int. J. Hydrog. Energy*, vol. 43, no. 33, pp. 16364–16372, Aug. 2018, doi: 10.1016/j.ijhydene.2018.06.166.

[7] L. Suneetha, P. Randive, and K. M. Pandey, 'Numerical investigation on implication of strut profile on combustion characteristics in a cavity based scramjet combustor', *Acta Astronaut.*, vol. 170, pp. 623–636, May 2020, doi: 10.1016/j.actaastro.2020.02.025.

[8] N. K. Mahto, G. Choubey, L. Suneetha, and K. M. Pandey, 'Effect of variation of length-to-depth ratio and Mach number on the performance of a typical double cavity scramjet combustor', *Acta Astronaut.*, vol. 128, pp. 540–550, Nov. 2016, doi: 10.1016/j.actaastro.2016.08.010.

[9] M. B. Sun, C. Gong, S. P. Zhang, J. H. Liang, W. D. Liu, and Z. G. Wang, 'Spark ignition process in a scramjet combustor fueled by hydrogen and equipped with multi-cavities at Mach 4 flight condition', *Exp. Therm. Fluid Sci.*, vol. 43, pp. 90–96, Nov. 2012, doi: 10.1016/j.expthermflusci.2012.03.028.
[10] I. B. Matveev, S. I. Serbin, and K. Wolf, 'Plasma-Assisted Ammonia Combustion—Part 1: Possibilities of Plasma Combustion of Ammonia in Air and Oxygen', *IEEE Trans. Plasma Sci.*, pp. 1–5, 2023, doi: 10.1109/TPS.2023.3273462.
[11] F. Tholin, 'Numerical simulation of nanosecond repetitively pulsed discharges in air at atmospheric pressure : Application to plasma-assisted combustion', phdthesis, Ecole Centrale Paris, 2012. Accessed: Oct. 10, 2022. [Online]. Available: https://tel.archives-ouvertes.fr/tel-00879856
[12] A. Vincent-Randonnier, V. Sabelnikov, A. Ristori, N. Zettervall, and C. Fureby, 'An expermiental and computational study of hydrogen-air combustion in the LAPCAT II supersonic combustor', *Proc. Combust. Inst.*, vol. 37, no. 3, pp. 3703–3711, 2019, doi: 10.1016/j.proci.2018.05.127.
[13] V. Sabelnikov *et al.*, 'Experimental investigation of plasma-assisted supersonic combustion', p. 8, 2017, doi: 10.13009/EUCASS2017-124.
[14] K. V. Savelkin, D. A. Yarantsev, and S. B. Leonov, 'Experiments on Plasma-Assisted Combustion in a Supersonic Flow: Optimization of Plasma Position in Relation to the Fuel Injector', *Aerosp. Lab*, no. 10, Dec. 2015, doi: 10.12762/2015.AL10-08.
[15] S. B. Leonov, A. Houpt, and B. Hedlund, 'Experimental Demonstration of Plasma-Based Flameholder in a Model Scramjet', in *21st AIAA International Space Planes and Hypersonics Technologies Conference*, Xiamen, China: AIAA Paper 2017-2249, Mar. 2017. doi: 10.2514/6.2017-2249.
[16] S. B. Leonov, S. Elliott, C. Carter, A. Houpt, P. Lax, and T. Ombrello, 'Modes of plasma-stabilized combustion in cavity-based M = 2 configuration', *Exp. Therm. Fluid Sci.*, vol. 124, no. 110355, Jun. 2021, doi: 10.1016/j.expthermflusci.2021.110355.
[17] E. Quemerais, 'Coupling with interpolation parallel interface'. [Online]. Available: https://w3.onera.fr/cwipi/
[18] A. Refloch *et al.*, 'CEDRE Software', *Aerosp. Lab*, no. 2, p. 1, Mar. 2011.
[19] G. Pelletier, 'Modélisation d'un foyer à combustion supersonique : simulations RANS et LES, comparaisons aux résultats expérimentaux', phdthesis, ENSMA, Palaiseau, 2022.
[20] C. J. Jachimowski, 'An analysis of combustion studies in shock expansion tunnels and reflected shock tunnels', NASA Langley Research Center Hampton, VA, United States, NASA-TP-3224, Jul. 1992. [Online]. Available: https://ntrs.nasa.gov/citations/19920019131
[21] S. Balay, W. Gropp, L. C. McInnes, and B. F. Smith, 'PETSc, the portable, extensible toolkit for scientific computation', *Argonne Natl. Lab.*, vol. 2, no. 17, 1998.
[22] A. D'Angola, G. Colonna, C. Gorse, and M. Capitelli, 'Thermodynamic and transport propertiesin equilibrium air plasmas in a wide pressure and temperature range', *Eur. Phys. J. D*, vol. 46, no. 1, pp. 129–150, Jan. 2008, doi: 10.1140/epjd/e2007-00305-4.
[23] A. Bourlet, J. Labaune, F. Tholin, A. Vincent, F. Pechereau, and C. O. Laux, 'Numerical model of restrikes in DC gliding arc discharges', in *AIAA SCITECH 2022 Forum*, San Diego, CA & Virtual: AIAA Paper 2022-0831, Jan. 2022. doi: 10.2514/6.2022-0831.
[24] A. Bourlet, J. Labaune, F. Tholin, A. Vincent-Randonnier, F. Pechereau, and C. O. Laux, 'Restrike model for an MHD solver: application to plasma assisted supersonic combustion in scramjet', 2022, doi: 10.13009/EUCASS2022-4549.
[25] S. B. Leonov, B. E. Hedlund, and A. W. Houpt, 'Morphology of a Q-DC Discharge within a Fuel Injection Jet in a Supersonic Cross-Flow', in *2018 AIAA Aerospace Sciences Meeting*, in AIAA SciTech Forum, AIAA Paper 2018-1060, 2018. doi: 10.2514/6.2018-1060.
[26] S. Kobayashi, Z. Bonaventura, F. Tholin, N. A. Popov, and A. Bourdon, 'Study of nanosecond discharges in H2–air mixtures at atmospheric pressure for plasma assisted combustion applications', *Plasma Sources Sci. Technol.*, vol. 26, no. 7, p. 075004, Jun. 2017, doi: 10.1088/1361-6595/aa729a.
[27] S. Elliott, P. Lax, S. B. Leonov, C. Carter, and T. Ombrello, 'Acetone PLIF visualization of the fuel distribution at plasma-enhanced supersonic combustion', *Exp. Therm. Fluid Sci.*, vol. 136, no. 110668, Aug. 2022, doi: 10.1016/j.expthermflusci.2022.110668.